Advanced Functional Materials

ADVANCED FUNCTIONAL MATERIALS
www.afm-journal.de

RESEARCH ARTICLE OPEN ACCESS

Achieving High ON State Current through Ferroelectric Polarization-Dependent Interfacial Resistance Switching in Undoped Orthorhombic HfO_2 Films

Markus Hellenbrand[1] | Nuno Estrócio[2,3] | Ji S. Kim[1] | Babak Bakhit[1] | Marian C. Istrate[4] | Corneliu Ghica[4] | Tiago Rebelo[2] | Nives Strkalj[5] | Abin Varghese[1,6] | Bernardo Almeida[2,3] | Luís S. Marques[2,3] | Bipin Rajendran[6] | Judith L. MacManus-Driscoll[1] | José P. B. Silva[2,3]

[1]Department of Materials Science and Metallurgy, University of Cambridge, Cambridge, UK | [2]Physics Center of Minho and Porto Universities (CF-UM-UP), University of Minho, Campus de Gualtar, Braga, Portugal | [3]Laboratory of Physics for Materials and Emergent Technologies, LapMET, University of Minho, Braga, Portugal | [4]National Institute of Materials Physics, Magurele, Romania | [5]Center for Advanced Laser Techniques, Institute of Physics, Zagreb, Croatia | [6]Department of Engineering, Faculty of Natural, Mathematical & Engineering Sciences, King's College London, Strand, London, UK

Correspondence: Markus Hellenbrand (mkhh2@cam.ac.uk) | Judith L. MacManus-Driscoll (jld35@cam.ac.uk) | José P. B. Silva (josesilva@fisica.uminho.pt)

Received: 19 December 2025 | **Revised:** 17 February 2026 | **Accepted:** 19 February 2026

Keywords: ferroelectric tunnel junctions | hafnium oxide | HfO_2 | neuromorphic functionality

ABSTRACT

In this work, we report on a ferroelectric tunnel junction based on an epitaxial undoped orthorhombic 3-nm-thin HfO_2 film. An OFF/ON resistance ratio of ≈83 and a high ON state current density of ≈5 A/cm^2, important for fast device readout, is achieved through ferroelectric polarization switching, which causes electron accumulation and depletion in the adjacent LSMO electrode. Oxygen vacancy movement inside the HfO_2 is observed, but plays at most a minor role for switching. The devices show stable switching endurance of over 10^6 switching cycles, low write voltages of ±3 V, both outperforming previous epitaxial HfO_2 FTJs, 16 measured resistance states, and neuromorphic capability by voltage pulse trains and spike-timing-dependent plasticity. This strong performance is achieved by designing ferroelectric tunnel junctions at the materials level of undoped HfO_2, which has a higher tunneling probability than HZO and a stabilized oxygen distribution. The resulting device design shows great promise for neuromorphic and analog memory applications.

1 | Introduction

In an era defined by fast and constant technological advancement, memory systems have ceased to be mere storage units and have become the backbone of technological progress, enabling devices to collect, process, and transmit information simultaneously. Traditional memory technologies such as DRAM and NAND flash, although highly versatile, struggle to meet the growing demands of modern applications [1–5]. A particularly urgent issue is the limited speed of data transfer between the processor and memory in traditional memory systems, referred to as the von Neumann bottleneck. This issue significantly impacts the system's performance in modern data-intensive applications such as artificial intelligence, machine learning, and real-time processing, where rapid access to large datasets is essential.

To overcome these limitations, research is increasingly focusing on brain-inspired architectures [6–11]. Drawing inspiration from the biological principles of the human brain, these systems enable in-memory computing by performing calculations directly within

---

Markus Hellenbrand and Nuno Estrócio contributed equally to this work.

Advanced Functional Materials, 2026; 0:e74667
https://doi.org/10.1002/adfm.74667

memory arrays, thereby reducing latency and energy consumption associated with data access. Several emerging technologies that are being actively investigated include the use of resistive switching (RS), ferroelectric (FE), phase-change, and spintronic materials [6–9, 12, 13]. In this context, ferroelectric materials are attracting considerable attention due to the possibility of switching the ferroelectric polarization under an applied electric field without significant mass transport. For instance, a ferroelectric tunnel junction (FTJ) is a resistance switching memory with low operation energy, high operation speed, and nondestructive readout capability [14]. In an FTJ, a thin ferroelectric barrier layer (<5 nm thick) is placed between two conductive electrodes with different electronic screening lengths. The charge accumulation in the electrodes and the height of the tunnel barrier will be affected when the ferroelectric polarization is switched, and this will produce a tunnel electroresistance (TER) with a considerable OFF/ON resistance ratio [15]. While HfO_2-based FE capacitors have been explored primarily for non-volatile memories [16–20] and energy-related applications [20–22], there is an increasing interest in leveraging ferroelectricity within FTJs [23, 24]. HfO_2-based materials have garnered increased attention for FTJs due to their robust FE properties, which arise from the presence of a metastable polar orthorhombic (*o*-) or rhombohedral (*r*-) phase with the space group $Pca2_1$ or R3m, respectively [25]. A key challenge for HfO_2 is that the stabilization of the *o*-phase in thin films often requires careful control of oxygen vacancy distributions, which can also facilitate the formation of conductive filaments in RS devices. This creates an interplay between ferroelectricity and filamentary RS [26–28], and thus, further investigation is needed to unravel the FTJ mechanism in *o*-phase HfO_2-based devices. HfO_2 stands out further as a prime memory material due to its excellent scalability, fast switching speed, low power operation, compatibility with CMOS technology, and ability to adopt multiple resistance states, enabling multi-level storage and neuromorphic capabilities [29–31].

Different FTJ configurations have been explored so far, most of them based on conducting electrodes such as TiN, Pt, and W. These FTJs typically show low ON/OFF current ratios (<20) [32, 33], while high ON/OFF ratios, typically in the range of 10^2–10^6, have been demonstrated in FTJs with n-type Si bottom electrodes [34–36]. However, large write voltages are needed due to the voltage drop across the interfacial barrier [36].

Recently, it was demonstrated that epitaxial films based on $Hf_xZr_{1\text{-}x}O_2$ (HZO) are crucial to understanding displacive and ionic phenomena [33], which govern FTJ performance. However, a high tunneling current in the ON state is needed to ensure that a scaled device can be read rapidly [35]. To achieve that, the thickness of HfO_2 in the FTJ needs to be reduced to the ultra-thin limit for adequate tunnel currents. However, further thickness reduction can result in an increase of the depolarization field and domain wall pinning, hence a reduction of polarization value and increase of coercive field, which degrade FTJ operation [37, 38]. Therefore, a compromise needs to be found. HZO epitaxial films have been investigated extensively as FTJs [39, 40]. Further work on this area requires higher ON-state currents to be reached with low write voltage and high endurance. On the other hand, undoped HfO_2 has not been investigated to a similar extent, and it is important to understand if it can offer improvements over HZO.

In this work, we demonstrate an FTJ based on FE switching of 3-nm-thin undoped epitaxial *o*-phase HfO_2 with switching voltages of ±3 V, switching endurance $>10^6$ cycles, 16 resistance levels, and neuromorphic functionality. All of this is achieved by stabilizing the oxygen vacancy concentration and consequently the FE *o*-phase of HfO_2, both without doping. Oxygen vacancy movement is observed to coexist with FE switching after repeated bias application with the same polarity, likely due to oxygen exchange between HfO_2 and the electrodes, but this does not have a significant effect on the resistance switching, demonstrating the stabilized oxygen vacancy concentration. We also demonstrate that FE switching controls the direct tunnelling current through the HfO_2 thin film on top of the $La_{0.67}Sr_{0.33}MnO_3$ (LSMO) electrode layer by modulating the LSMO carrier accumulation and depletion. Temperature-independent switching performance up to 150°C confirms the fully tunnelling-controlled mechanism.

2 | Experimental Details

Single-crystal (001)-oriented Nb:STO with 0.7 wt.% doping and a resulting electronic conductivity at room temperature >143 S/cm was used as the substrate. A 13 nm LSMO layer was deposited by pulsed laser deposition (PLD) with a KrF excimer laser with a wavelength of 248 nm, as a buffer, as commonly adopted in the literature to enhance the FE properties [41]. Then, a 3 nm undoped HfO_2 film was deposited subsequently by PLD. The LSMO layer was grown at a substrate temperature (T_s) of 710°C, oxygen pressure (pO_2) of 0.1 mbar, pulse energy of 150 mJ, and with a laser repetition rate of 3 Hz. The HfO_2 film was deposited under the same pO_2 and pulse energy, but with a T_s of 720°C and repetition rate of 2 Hz. The distance between the substrate holder and the target was set at 4.5 cm for the LSMO deposition and 5.0 cm for the HfO_2 deposition. X-ray diffraction (XRD) characterization was carried out with a PANalytical Empyrean Diffractometer at room temperature over a 2θ range of 20–34° in a Bragg-Brentano configuration using CuK_α radiation ($\lambda = 1.5406$ Å). For electrical characterization, 50-nm-thick circular tungsten (W) top electrodes (TEs) with diameters of 25, 50, and 100 µm were deposited by sputtering and a UV lithography lift-off process. Electrical characterization was carried out in a manual EverBeing probe station with a thermal sample stage, together with a computer-controlled [42] Keysight B2912 source-measure unit. For fast pulse measurements, an MPI TS2000D semi-automated probe station and a Keysight B1500A parameter analyzer with waveform generator/fast measurement units were used. For low-frequency noise measurements, the source/measure units of the same parameter analyzer were used to record the current, followed by a fast Fourier transform to calculate the power spectral density as a function of frequency. For electrical measurements, the voltage was always applied to the TE, unless specified otherwise. Microstructural characterization of the sample was performed using high-resolution transmission electron microscopy (HRTEM) under conditions provided in previous work [43]. Depth-resolved X-ray photoelectron spectroscopy (XPS) measurements were conducted using a Thermo Scientific Escalab 250Xi instrument with monochromatic AlK_α radiation ($h\nu = 1486.6$ eV). Surface sputter-etching was performed with 200 eV Ar^+ ions. To minimize destructive effects on the XPS core levels during sputtering and to prepare electrodes for biasing the devices, W electrodes with an average thickness of

≈8 nm and diameters of ≈400 µm were sputter-deposited on the HfO_2/LSMO/Nb:STO surface. Devices in two different electrical states were chosen for XPS measurements: (i) a pristine device and (ii) a device that was positively biased with 500 voltage sweeps from 0 to +3.5 V applied to the TE. The binding energies of the spectra were calibrated against their Fermi edge cut-offs. Deconvolution of the Hf 4f core level spectra was carried out using the CasaXPS software after subtracting the Shirley-type background. The Hf 4f core level spectra were deconvoluted by keeping the $4f_{5/2}$-$4f_{7/2}$ binding energy separations at 1.6 eV, the full-width-at-half-maximum values at 1.6 eV, and the $4f_{5/2}$:$4f_{7/2}$ area ratios at 3:4, while peak positions and areas were changed. The line shapes were modelled as Gaussian-Lorentzian. Piezoresponse force microscopy (PFM) was performed using a Bruker Multimode 8 atomic force microscope with Pt-coated NSC35 tips (MikroMasch) with a spring constant of 5.4 N/m. The sample was mounted on a metallic disc where V_{DC} was applied to the bottom Nb:STO/LSMO whilst the Pt PFM tip was grounded. Both piezo-response force spectroscopy (PFS, "on field") and PFM poling ("off field") responses were detected using V_{ac} = 0.5 V at 900 kHz. PFS was performed on W electrodes of 20 µm diameter.

3 | Results and Discussion

3.1 | Structural Characterization

Figure 1a presents the XRD pattern of the HfO_2/LSMO/Nb:STO structure. The most intense peaks, at $2\theta = 22.7°$ and $2\theta = 23.1°$, correspond to the (001) planes refractions of the cubic Nb:STO substrate and the pseudo-cubic LSMO bottom layer, respectively. The diffraction peak at 29.73° ($d_{111} = 0.3$ nm) is indexed to the (111) planes of the *o*-HfO_2 film [44]. In epitaxy, the observation of Laue oscillations around the main peaks is often regarded as a quality mark for thin films. For ultra-thin films, however, their intensity is strongly decreased, as shown in previous work [45], and so their absence is not necessarily a sign of low-quality films. In addition, in thinner films such as this case (3 nm), the main (111) peak is very broad, which makes it impossible to distinguish between the d_{111} and $d_{11\text{-}1}$ peaks by using in-plane and out-of-plane XRD measurements to confirm the crystal phase. This was observed in previous work, too, in a 5 nm thick La:HfO_2 thin film [46]. For this reason, we have performed TEM experiments that conclusively confirm the presence of the *o*-phase in the HfO_2 pure films.

The HRTEM image in Figure 1b reveals the device structure comprising a top W electrode, a 3 nm HfO_2 layer, a 13 nm LSMO electrode, and the Nb:STO substrate. To reveal the degree of crystallization in the sample, a fast Fourier transform (FFT) was performed on the entire area shown in Figure 1b, and the result is presented in Figure 1c. The FFT pattern displays two distinct sets of peaks: one corresponding to the (111) planes of the HfO_2 lattice with an interplanar spacing of 0.302 ± 0.002 nm, consistent with the XRD results, and the other corresponding to the (001) planes of the Nb:STO lattice with an interplanar spacing of 0.391 ± 0.002 nm. It is worth noting that the lattice parameters of bulk Nb:STO and the pseudo-cubic LSMO structures are similar, leading to an overlap of the (001) pseudo-cubic LSMO and (001) Nb:STO peaks. A clear crystallographic relationship for the out-of-plane direction between the HfO_2 thin film, the LSMO electrode, and the Nb:STO substrate can be derived, specifically: [111] HfO_2 || [001] LSMO || [001] Nb:STO.

Figure 1d shows a high-resolution scanning TEM (HR-STEM) image of the HfO_2/LSMO interface, where the well-oriented LSMO electrode and the lattice fringes of the HfO_2 film are clearly visible. The HfO_2 fringes have a measured spacing of 0.301 ± 0.002 nm, corresponding to the (111) planes of HfO_2. To rule out the presence of the *r*-phase [47, 48] or *o*-phase with rhombohedral distortion [49], and confirm the presence of the *o*-phase, further TEM experiments were performed as explained in Note S1 and Figure S1. The HR-STEM image in Figure 1d further reveals a well-defined and high-quality interface between the HfO_2 thin film and the LSMO electrode, confirming the high crystallinity and quality of the deposited HfO_2 thin film.

While not regarded as immediately fab-friendly, the use of LSMO and an epitaxial process does not automatically disqualify a materials system from CMOS compatibility. The integration of LSMO/STO heterostructures on silicon by the use of buffer layers [50] or layer transfer [51] has already been demonstrated.

3.2 | Electrical Characterization

Figure 2a presents multiple current-voltage (*I–V*) curves measured across ten different devices with electrodes of 100 µm diameter, each subjected to five switching cycles.

The device structure is shown in the inset of the same figure, and the measurements were performed at room temperature, with voltages applied to the TE unless specified otherwise. Apart from excellent uniformity and repeatability, the *I–V* curves reveal the presence of two distinct resistance states (high resistance state HRS and low resistance state LRS) with low set and reset voltages of +3 and −3 V, respectively The devices exhibit an average ON/OFF current ratio of ≈83 ± 26, measured at a read voltage (V_{read}) of −0.1 V, all achieved without requiring a forming process. The pristine devices start in the HRS, switch to the LRS upon positive voltage application, and back to the HRS upon negative voltage application, as indicated by the arrows in Figure 2a.

In support of identifying the nature of the underlying RS mechanism in these devices, the dependence of the switching currents on the electrode diameter/area was studied, and a clear scaling of the currents with the device's size is observed, see Figure S2. Additionally, the behavior observed for the sample with increased LSMO thickness of 25 nm supports a switching mechanism that does not rely on the formation of filaments [52, 53], and this is supported further by the gradual changes in current when switching between HRS and LRS, rather than abrupt changes, which are typically observed in filamentary switching [54]. In addition, a high tunneling current density of ≈5 A/cm^2 at a read voltage of −0.1 V is achieved in the ON state, which can be further increased to ≈42 A/cm^2 at a read voltage of −0.5 V. This is desirable for high-speed operation and more than an order of magnitude higher than most HZO FTJs, summarized in Table S1. We achieved this higher ON current compared with HZO by exploiting the higher transmission probability through undoped HfO_2 [55], and the stabilized ferroelectricity in ultra-thin films.

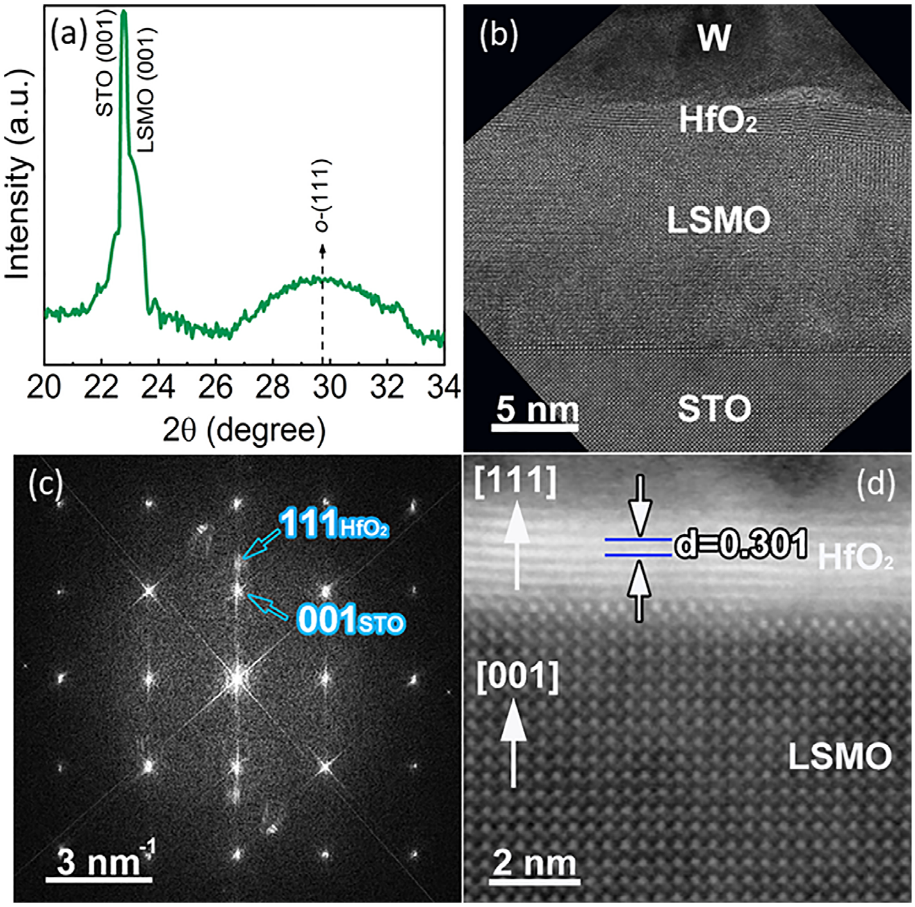

FIGURE 1 | Structural characterization of the HfO_2/LSMO/Nb:STO structure. (a) X-ray diffraction pattern (logarithmic y-scale) with marked Nb:STO, LSMO (001), and *o*-(111)HfO_2 peaks. (b) High-resolution transmission electron microscopy image with labels of the different layers. (c) Fast Fourier transform pattern corresponding to the image shown in (b). (d) High-resolution scanning transmission electron microscopy image recorded at the HfO_2/LSMO interface.

Figure 2b illustrates the repeatability of both HRS and LRS over 10^6 switching cycles, measured at $V_{\text{read}} = -0.1$ V. Despite an initial drift of the states, a stable memory window is maintained for up to the measured 10^6 cycles. The cause of this improved endurance when compared to previous works in epitaxial HZO FTJs, shown in Table S1, will be discussed later. In Figure S3, the cycling endurance was investigated further for increasingly fast programming pulses. With details provided in the SI, the devices still respond down to 20 ns programming pulses. While the electrode layout and measurement setup in this demonstration do not allow a real-time recording of the switching currents (see explanation with Figure S3), the switching energy can be estimated with a few well-supported assumptions. If the actual switching currents without transients remain the same at the fastest measured switching speeds as in the I–V measurement in Figure 1a, given that the device currents scale with the electrode area, devices at back-end-of-the-line dimensions (e.g. 20 × 20 nm^2) can be expected to switch with nanoampere currents, resulting in a switching energy consumption on the order of femtojoule, comparable to SRAM cells [56].

Figure 2c shows that the device current can be modulated by subsequent voltage pulses with different amplitudes. So as not to overload the figure, the currents associated with the switching voltages were omitted, leaving only the read currents recorded at −0.1 V. The results show good repeatability and reveal that the current can be modulated over more than an order of magnitude.

Figure 2d highlights the multi-level retention capabilities of the devices, measured for up to 900 s. Despite an initial decay of some of the states, they stabilize to 16 separate states. Extended retention measurements of >10^4 s for the highest and lowest resistance states are presented in Figure S4.

Finally, the neuromorphic capabilities of the fabricated devices were evaluated by conducting spike-timing-dependent plasticity (STDP) measurements to emulate the behavior of biological synapses. The neuromorphic voltage profiles, shown in the inset of Figure 3a, consisted of a sum of two symmetric voltage signals, representing pre-synaptic and post-synaptic spikes, which were systematically shifted in time relative to each other. Each spike was composed of two inverted triangular segments with varying amplitudes. After the application of the time-shifted voltage profiles, the resulting state was measured by 100 points with $V_{\text{read}} = -0.1$ V, and each time shift was measured 10 times. The values presented in Figure 3 correspond to the averages of these 10 repetitions. Error bars were derived using standard error propagation based on the standard deviations of the 100-point averages and ten repetitions. Further details on the voltage profiles can be found in previous work [53].

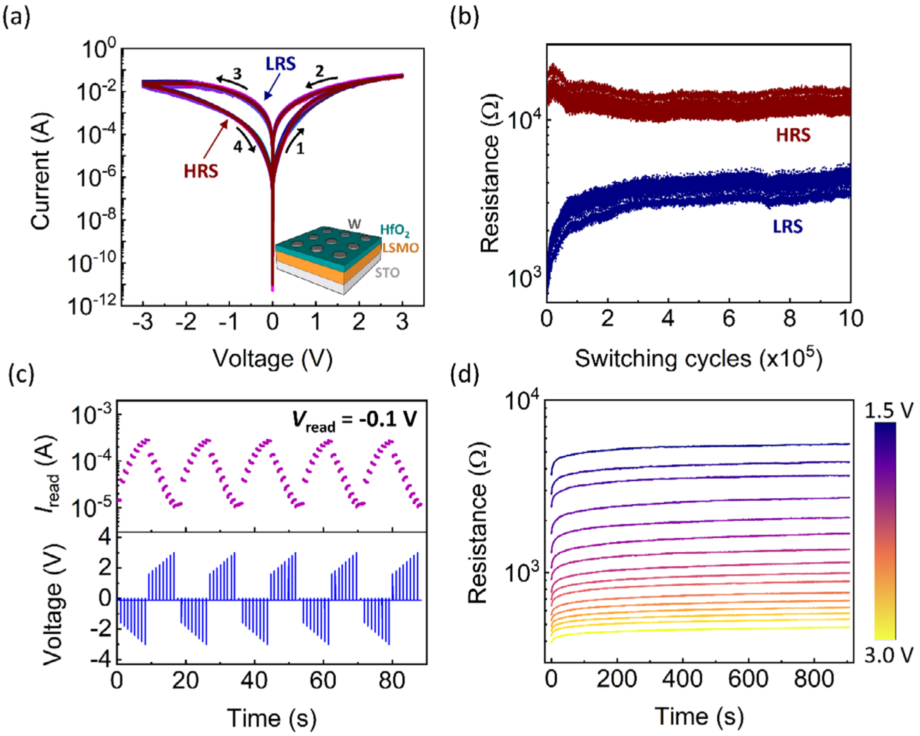

FIGURE 2 | Electrical characterization of the W/HfO_2/LSMO/Nb:STO devices. (a) Current-voltage (I–V) curves were measured from ten different devices with electrodes of 100 µm diameter, each subjected to five switching cycles (50 curves in total). (b) Switching endurance, where the resistance values of LRS (blue) and HRS (red) were measured at $V_{read} = -0.1$ V as a function of the number of switching cycles, up to 10^6 cycles. (c) Read current modulation (top panel, $V_{read} = -0.1$ V), achieved by applying subsequent voltage pulses of varying amplitudes (bottom panel). (d) Multiple-state resistance retention over 900 s for programming voltages ranging from 1.5 to 3.0 V without intermediate reset. $V_{read} = -0.1$ V. Note that for (c) and (d), the voltage was applied at the bottom electrode.

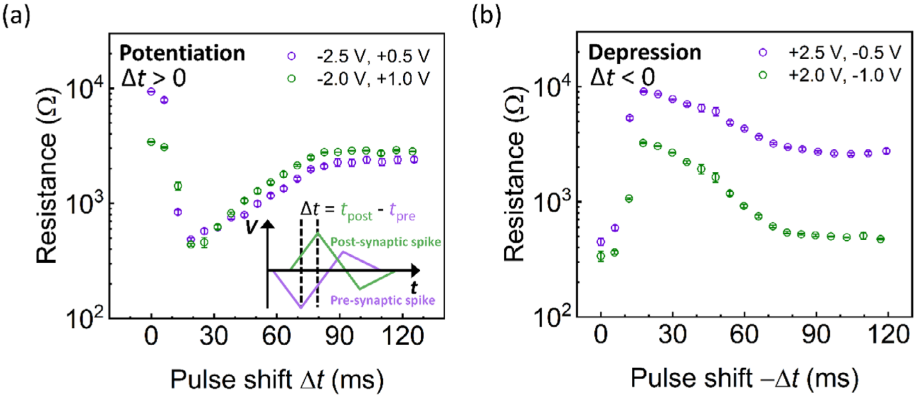

FIGURE 3 | Neuromorphic characterization of the fabricated devices using spike timing-dependent plasticity measurements. (a) Potentiation profile observed when the pre-synaptic spike precedes the post-synaptic spike. Inset: Schematic of the neuromorphic voltage profiles, which consist of the sum of two mirrored voltage signals shifted in time relative to each other: the pre-synaptic spike (purple) and the post-synaptic spike (green). (b) A depression profile is observed when the pre-synaptic spike arrives after the post-synaptic spike. The legend of each data set in each plot specifies the polarity and amplitude of the two triangular segments composing the synaptic pulses.

The apparent synaptic modulation confirms the ability of the fabricated devices to successfully emulate STDP, underscoring their potential for neuromorphic applications.

In the case where the pre-synaptic spike arrives before the post-synaptic spike, potentiation occurs, as illustrated in Figure 3a, indicating the strengthening of the synapse (decrease of the resistance). Conversely, when the pre-synaptic spike follows the post-synaptic spike, depression occurs, as shown in Figure 3b, representing weakening of the synapse (increase of the resistance). In each measurement, two pairs of different amplitudes were used for the triangular segments, as indicated in the legends

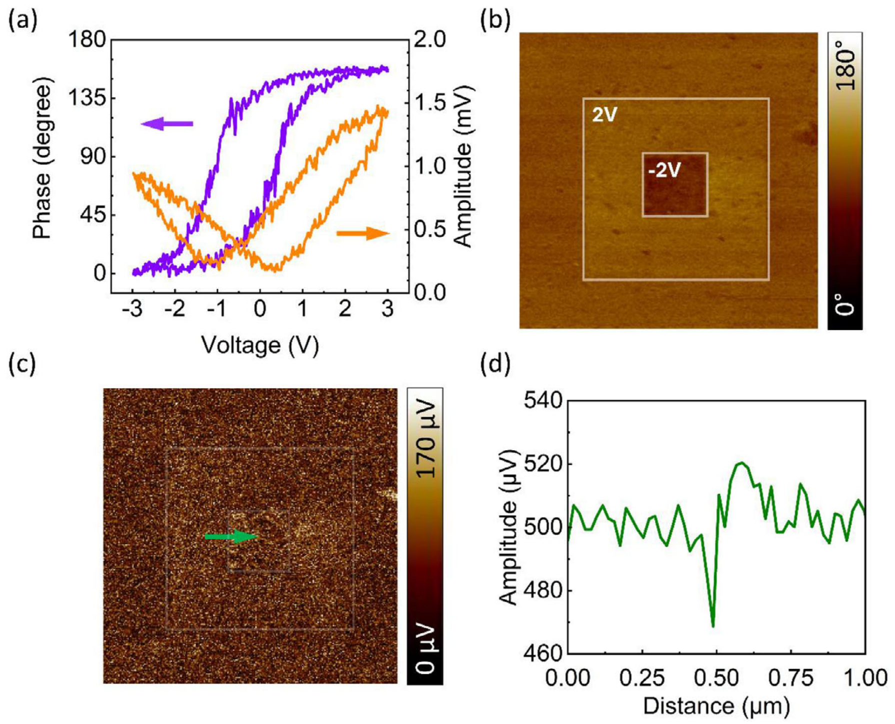

FIGURE 4 | Piezo-response force spectroscopy/microscopy of the HfO_2/LSMO/Nb:STO structure. (a) Phase (purple) and amplitude (orange) signals from piezo-response force spectroscopy (PFS). Nearly 180° of phase change was observed between −3 and 3 V. (b) Phase response from vertical piezo-response force microscopy (v-PFM). Clear contrast is observed between 2 and −2 V poling. (c) Amplitude response from v-PFM. (d) Amplitude mapping of the amplitude response from PFM along the green arrow in (c). A sharp fluctuation of the amplitude was observed at the boundary between oppositely poled polarizations, indicative of a domain wall between the oppositely polarized areas.

of Figure 3a,b. This illustrates how the general STDP functionality can be tuned further for stronger or weaker effects.

3.3 | Ferroelectric Characterization

The observation of resistance switching in *o*-HfO_2 beckons the question of whether ferroelectricity is responsible for the electrical behavior. In addition, ferroelectricity has rarely been observed in undoped HfO_2 films as thin as 3 nm, which makes the investigation even more worthwhile. To investigate the presence of ferroelectricity in the *o*-HfO_2 thin film, piezo-response force spectroscopy (PFS) and piezo-response force microscopy (PFM) were performed, using Pt-coated probe tips (see Experimental Details). PFM poling was performed on the bare HfO_2 film surface, while PFS was performed on W TEs of 25 µm in diameter.

Out-of-plane PFS was performed with V_{DC} of ±3 V (same as current-voltage measurements) for writing and V_{ac} of 0.5 V at 900 kHz. The phase and amplitude signals from PFS are plotted in Figure 4a. There is a slight shift of the phase hysteresis loop towards negative voltages due to the asymmetric film stack, i.e., a bottom contact of LSMO/Nb:STO, while the top contact consisted of W. A coercive voltage of ≈0.8 V was obtained from the minima (≈0.4 and ≈-1.2 V) of the amplitude loop, and a nearly 180° phase change was observed between −3 and 3 V, indicative of bi-axial switchable polar states. A low writing voltage is expected to result from this low coercive voltage. Figure 4b,c shows the phase and amplitude response, respectively, from vertical PFM (v-PFM), with V_{DC} of ±2 V for writing and V_{ac} of 0.5 V for reading. The phase contrast in Figure 4b indicates reversible, spatially oppositely polarized states, while the unpolarized pristine states show a multi-domain pattern. The amplitude response in Figure 4c is weak due to the small thickness and low d_{33} piezo-response of a few pm/V for HfO_2 films compared with perovskite ferroelectrics with up to several hundred pm/V [57, 58]. The current through the thin films here is not a leakage current, but constitutes the key functionality of the devices. Therefore, methods of current compensation are not applicable to try to extract the transient currents due to polarization switching. In Figure 4d, the amplitude along the green arrow in Figure 4c is plotted against the distance. A sharp fluctuation of the amplitude was observed at the boundary of two oppositely polarized regions, indicative of a domain wall.

In order to gauge if the observed phase contrast is driven by charge injection instead of ferroelectricity, a retention measurement was performed for 3600 s, shown in Figure S5. Generally, for HfO_2, the lifetime of injected charge is ~1000 s [59], but for the present HfO_2 films, the phase contrast was retained even after 3600 s, indicative of non-volatile polar states rather than a charge injection effect. Similarly, the domain wall is retained in the amplitude signal, which is further evidence of the retention of opposite polar states.

3.4 | Compositional Characterization

Before relating the observed ferroelectricity to the resistance switching, depth-resolved X-ray photoelectron spectroscopy (XPS) measurements on both the HRS and LRS states will be

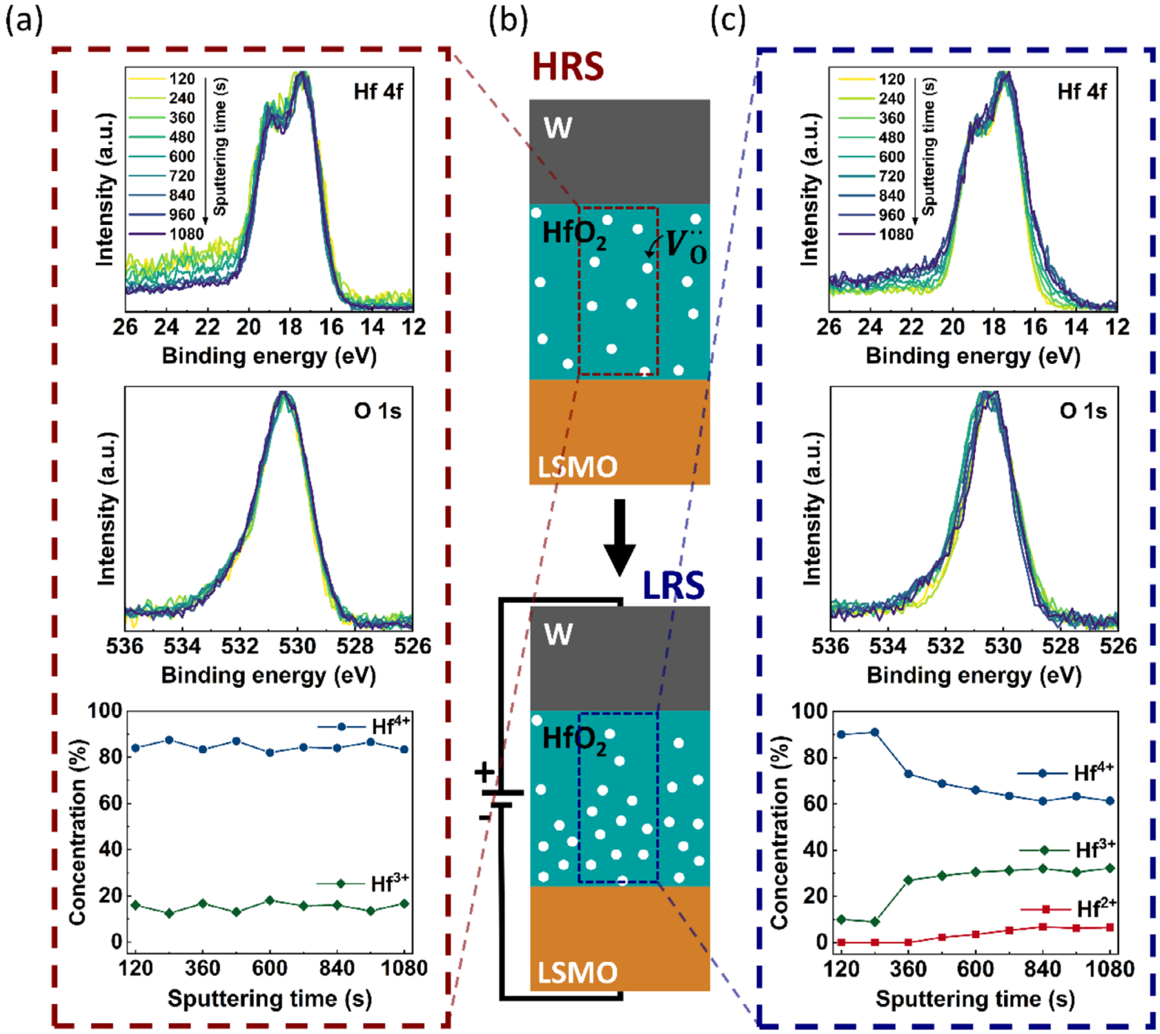

FIGURE 5 | X-ray photoelectron spectroscopy, chemical characterization, and oxygen redistribution schematic for the W/HfO_2/LSMO/Nb:STO structure. (a) Hf 4f (top) and O 1s (middle) core level spectra, and the concentration of Hf^{4+} and Hf^{3+} as a function of sputtering time (bottom) for the pristine HRS. (b) Illustration of the oxygen redistribution after biasing. (c) Hf 4f (top) and O 1s (middle) core level spectrum, and the concentration of Hf^{4+}, Hf^{3+}, and Hf^{2+} as a function of sputtering time (bottom) for the LRS after 500 positive *I*–*V* cycles. The increase in Hf suboxides with increasing etching time can be derived from the increasing low-energy shoulder observed in the Hf 4f core level spectra.

discussed to reveal different Hf oxidation states in the two resistance states. Figure 5a,c show the Hf 4f (top figures) and O 1s (middle figures) core level spectra acquired from devices in the pristine HRS (a) and positively biased LRS (c) – 500 *I*–*V* sweeps from 0 to 3.5 V at the TE – as a function of sputter etching time *t* of the top W surface. For these measurements, the W top metal was ≈8 nm thin to serve as an electrode and cap layer to allow acquiring the Hf 4f signals at different depths without damaging them by sputter-etching [53] (only the W was etched by sputtering, and with decreasing W thickness, increasing depths into the HfO_2 were probed). The signal intensities were normalized to show possible changes in peak positions and shapes. For both cases, the Hf 4f and O 1s signals appear at the same positions, indicating that there is no detectable chemical shift as a function of depth. While the shape of the Hf 4f spectra does not change throughout the HfO_2 layer in the pristine device, see Figure 5a, a shoulder appears at the lower binding energies of the Hf 4f spectra for the biased device, see Figure 5c. The area under this shoulder increases up to $t = 600$ s, then remains constant for $t \geq 720$ s. Since the XPS core levels of the 3 nm HfO_2 layer were acquired while the W top layer was still present (but gradually thinned in the etching process), the observed shoulder in the Hf 4f spectra does not originate from Ar ion sputter damage, but can be attributed to the formation of reduced Hf oxidation states during the switching process [53]. Furthermore, it is clear that this difference appears due to the electrical bias, rather than sputter damage, as the pristine HRS and biased LRS devices were subjected to the same etching procedure, but yielded different Hf 4f core level spectra.

The Hf 4f peaks were deconvoluted to obtain the impact of applying a positive bias on the Hf oxidation states in HfO_2. For the pristine condition, the Hf 4f spectra were fitted with two doublets, corresponding to the existence of Hf^{4+} and Hf^{3+}, see Figure S6a for details. It is well established that the proportion of Hf^{3+} serves as a quantitative indicator of the oxygen vacancy concentration [60], and the existence of oxygen vacancies seems essential to achieve *o*-phase HfO_2 films [26]. The concentration of the lower

Hf oxidation states does not significantly change throughout the HfO_2 layer: ≈82% Hf^{4+} and ≈18% Hf^{3+}, as presented in Figure 5a, bottom figure. This demonstrates a stable and uniform oxygen vacancy concentration in these devices, achieved simply by ultrathin films without doping, and this leads to the uniform and stable electrical performance with high endurance and uniformity. The stable epitaxial films are so thin that even oxygen, which might be scavenged from the electrodes, cannot create an oxygen gradient in the film, and therefore oxygen drift and diffusion are suppressed, leading to stable switching performance.

The Hf 4f spectra acquired from the positively biased device, however, consist of an additional doublet corresponding to Hf^{2+}, see Figure S6b. Figure 5c, bottom figure, shows the concentrations of Hf^{4+}, Hf^{3+}, and Hf^{2+} as a function of sputter etching time t. For $t > 360$ s, while there is a downward trend in the Hf^{4+} concentration, the concentrations of Hf^{3+} and Hf^{2+} steadily increase toward the HfO_2/LSMO interface.

The same changes would be expected for the O 1s core level spectra. However, the normalized O 1s spectra shown in Figure 5a,c, middle figures, consist of peaks with similar widths and shapes, with no chemical shift or visible peak splitting. This is mainly because the O 1s peaks with different oxidation states appear at very close binding energies, and the variations in the fractions of their oxidation states are not sufficiently high to change the peak shapes [53]. Figure 5b presents a visual representation, based on the XPS results, illustrating the distribution of oxygen vacancies in the two resistance states. In the pristine state, the device is in the HRS, and an oxygen vacancy concentration corresponding to <20% Hf^{3+} is uniformly distributed within the HfO_2 film. After the repeated application of a positive voltage to the W TE, an increased oxygen vacancy concentration is measured in the HfO_2, coinciding with a switch from the pristine HRS to the LRS.

In the absence of any other atomic species, the change in Hf 4f oxidation states reveals the movement of oxygen within our devices after excessive biasing with the same polarity. If the oxidation states are reduced in the HfO_2 layer, oxygen has to move into and out of the BE and/or TE. It has been reported that there can be oxygen exchange between LSMO and HfO_2-based ferroelectrics [61], but the voltage polarity does not fit here. A positive voltage at the TE should draw negatively charged oxygen ions out of the LSMO, not oxygen vacancies, and this would increase the Hf oxidation state, not reduce it, as observed here. On the other hand, it is known that W, which is the TE in our devices, or an interfacial WO_x layer, formed during switching, can be reversibly oxidized under bias application [62], and oxygen exchange with the TE has been reported even for noble metals such as Pt [63]. In the latter case, the TE serves as an oxygen reservoir without oxidation reactions of the metal. While we could not resolve whether the W oxidizes during switching, as the W core level overlaps with Hf, given the observed *I–V* polarity, oxygen exchange with the W electrode seems more likely. Nevertheless, this is only observable after 500 consecutive positive *I-V* sweeps, very different from the actual device operation. Hence, this small effect and the observed one order of magnitude higher endurance than most epitaxial HZO FTJs indicate a stable oxygen distribution in normal device operation. Thus, the ferroelectric switching with minimal mass transport is by far the dominant switching mechanism, with at most a potential secondary, minor contribution from the movement of oxygen between the HfO_2 and the TE.

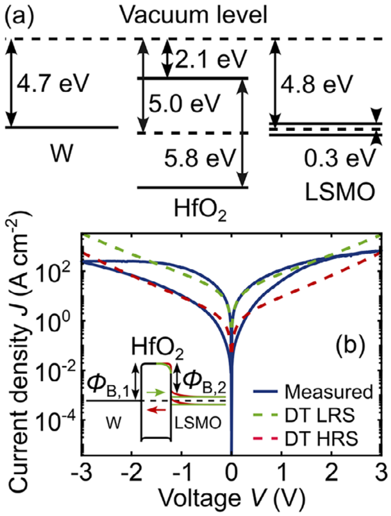

FIGURE 6 | Band diagram and electronic conduction mechanism. (a) Work function and band gap literature values for W, HfO_2, and LSMO. (b) Measured current density (100 µm TE diameter) and calculated direct tunneling (DT) current density according to (1). The analytical expression accurately reproduces the correct order of magnitude of the current density without a free fitting parameter. Inset: Band diagram according to the Schottky-Mott rule when the materials with values as in (a) are brought into contact. The colored (online) arrows indicate the direction of polarization. The change in band bending depending on polarization is only illustrated on the side of the LSMO interface, as this is the current-limiting element. The effect on the opposite interface is negligible.

3.5 | Electronic Conduction and Resistance Switching Mechanism

In the following, the electrical device behavior will be discussed in light of the measured ferroelectric switching and oxygen vacancy concentrations. For a HfO_2 oxide layer as thin as 3 nm, direct tunnelling can be expected to be the dominant electronic current mechanism, and its current density J_{DT} can be calculated analytically according to [64]:

$$J_{\mathrm{DT}} = C\,\frac{\exp\left[\alpha\left\{\left(\Phi_{\mathrm{B},2}-\frac{qV}{2}\right)^{3/2}-\left(\Phi_{B,1}-\frac{qV}{2}\right)^{3/2}\right\}\right]}{\alpha^{2}\left\{\sqrt{\Phi_{B,2}-\frac{qV}{2}}-\sqrt{\Phi_{B,1}+\frac{qV}{2}}\right\}^{2}}$$

$$\times\sinh\left[\frac{3qV}{4}\alpha\left\{\sqrt{\Phi_{B,2}-\frac{qV}{2}}-\sqrt{\Phi_{B,1}+\frac{qV}{2}}\right\}\right] \qquad (1)$$

where $C = -4qm_{\mathrm{ox}}/(9\pi^2\hbar^3)$, $\alpha = 4d\sqrt{2m_{ox}}/[3\hbar(\Phi_{\mathrm{B},1}+qV-\Phi_{\mathrm{B},2})]$, $\Phi_{B,1}$ and $\Phi_{B,2}$ are the barrier heights according to Figure 6, q is the elemental charge, V is the voltage applied across the barrier, and $m_{\mathrm{ox}} = 0.11\times m_0$ for HfO_2 [65], where m_0 is the electron rest mass. Figure 6a and the inset of Figure 6b present the expected band diagram of our devices according to the Schottky-Mott rule. With literature values [66–69] for all parameters in (1), provided in Figure 6a, and without any free fitting parameters, the calculated J_{DT} according to (1) lands right on top of the measured LRS currents and accurately reproduces the correct order of magnitude, see Figure 6b. The only assumption is for the Fermi level in $\mathrm{HfO_2}$ to lie in the middle of the band gap, and the resulting electron affinity of 2.1 eV is in agreement with experimental values [65]. In addition, even with a variation of the barrier height of a few hundred meV, the order of magnitude of the current density is still reproduced correctly, so the assumption of a mid-gap Fermi level is not critical. The deviations of the measured current density from the ideal analytic equation can be explained by the presence of secondary electronic conduction mechanisms and a series resistance from, e.g., the LSMO/Nb:STO.

The current density expected from the reverse Schottky emission equation, as another typically observed electronic conduction mechanism in metal-insulator-metal structures [64], is several orders of magnitude lower than the measured currents due to the high values of $\Phi_{\mathrm{B},1}$ and $\Phi_{\mathrm{B},2}$ in Figure 6b. Alternatively, if the reverse Schottky equation is fitted to the measured data, it results in barrier heights of 0.54 and 0.38 eV for the HRS and LRS, respectively, although the fits do not match the measured *I*–*V* curves well (see Figure S7). While these barrier heights could be explained in principle by strong Fermi level pinning due to trap levels high up in the band gap of the $\mathrm{HfO_2}$, the only other fitted value, the high-frequency dielectric constant, yields values of 6–8 (HRS) and 35–39 (LRS), which is much higher than experimental literature values of ≈2–3 [70] and thus makes this interpretation unphysical. In addition, if the conduction band was pinned in this way, the expected current density according to (1), contributing at the same time, would be orders of magnitude higher than the measured values, see Figure S8. Fowler-Nordheim tunneling as the third candidate [64] for electronic conduction in the presented structure did not fit the measured *I*–*V* curves.

To corroborate this understanding, temperature-dependent *I*–*V* measurements and low-frequency noise (LFN) measurements were carried out. The former are presented in Figure S9 and reveal that neither the switching mechanism nor the electronic conduction is thermally activated. The latter (LFN) are presented in Figure S10 and reveal frequency-independent LFN, which is what would be expected for tunneling shot noise. Other conduction mechanisms, such as Poole-Frenkel emission, have been shown to exhibit $1/f$ characteristics of LFN, and indeed, it has been shown that in FTJs where both tunneling and PF emission are present, the LFN characteristics differ between $1/f$ and frequency-independent, respectively [71, 72]. Both the temperature-dependent and LFN observations are in line with the understanding of ferroelectric switching and direct tunneling.

With direct tunnelling as the most likely electronic conduction mechanism, the resistance switching mechanism can be explained in more detail. Again, based on (1), it turns out that a change of $\Phi_{\mathrm{B},1}$ and $\Phi_{\mathrm{B},2}$ upon polarization reversal does not lead to a significant change in the current levels. This is explained because tunneling occurs close to the Fermi level (or conduction band minimum for semiconductors), where the effective barrier height for a trapezoidal tunneling barrier remains similar upon change of $\Phi_{\mathrm{B},1}$ and $\Phi_{\mathrm{B},2}$ (up to a value similar to the offset between both sides). Instead, the tunneling current strongly depends on the tunneling distance d. With an increase of as little as 0.4 nm, i.e., increasing d from the film thickness of 3 nm to an effective thickness of 3.4 nm in (1), the measured HRS current is reproduced almost as closely as the LRS. Such an increase in the effective tunneling distance can occur due to electron depletion in the LSMO for a polarization pointing away from it, as illustrated in the inset of Figure 6, and this is consistent with the switching orientation of the measured *I*–*V* curves.

The value of 0.4 nm can be checked by estimating the depletion width inside the LSMO as a consequence of the FE polarization of the $\mathrm{HfO_2}$. In a metal-insulator-semiconductor structure, the depletion width w_{D} in the semiconductor can be estimated as $w_{\mathrm{D}} = \sqrt{2\varepsilon_0\varepsilon_{\mathrm{s}}\Psi_{\mathrm{s}}/(qN)}$, where ε_0 and ε_{s} are the vacuum and semiconductor permittivity, respectively, Ψ_{s} is the built-in voltage at the semiconductor interface, q is the elemental charge, and N is the carrier concentration in the semiconductor [73]. Formally, a change in w_{D} due to a change in Ψ_{s} due to FE polarization would hence be $\Delta w_{\mathrm{D}} = \sqrt{2\varepsilon_0\varepsilon_{\mathrm{s}}/(qN)} \times [\sqrt{\Psi_{\mathrm{s}} + \Delta\Psi_{\mathrm{s}}} - \sqrt{\Psi_{\mathrm{s}}}]$. With literature values of $\varepsilon_{\mathrm{s}} \approx 30$ [74] and $N = 10^{21}$–$10^{22}\ \mathrm{cm^{-3}}$ [75], and with the approximation that the conduction band edge in the $\mathrm{HfO_2}$ and LSMO changes by the same amount, $\Delta\Psi_{\mathrm{s}} \approx \sigma\delta/(\varepsilon_0\varepsilon_{\mathrm{s}})$ [76], where σ is the additional interface charge due to the FE polarization P, i.e., $\sigma = P$. Due to the high device currents, it was not possible to measure the polarization directly, but for similar films in previous work, it was estimated that $P \approx 10\ \mu\mathrm{C/cm^2}$ [28]. With the provided values, if for simplicity it is assumed that $\Psi_{\mathrm{s}} \approx 0$, the equation for w_{D} yields values between 0.2 and 0.8 nm for N between 10^{22} and $10^{21}\ \mathrm{cm^{-3}}$, respectively, which is in good agreement with the value of 0.4 nm from the direct tunnelling equation. When assuming that $\Psi_{\mathrm{s}} \approx 2\Delta\Psi_{\mathrm{s}}$ as an upper-bounds reference, w_{D} reduces to 0.1–0.3 nm, which is in good agreement, too. Obviously, condensing the change between LRS and HRS into just this one number is a simplification [74], but it yields consistent estimations. A change in the LSMO depletion width can also explain the slight asymmetry between the two branches of the HRS. In the LRS, where there is no additional depletion width present in the LRS, the $\mathrm{HfO_2}$ barrier appears roughly symmetric for positive and negative bias. In the HRS, however, with an additional depletion width in the LSMO, the barrier appears asymmetric for different voltage polarities.

A potential effect of oxygen exchange between the $\mathrm{HfO_2}$ and (likely) the W electrode would affect the $\mathrm{HfO_2}$ bands qualitatively in the same way by gradually lowering the effective tunneling barrier height for gradual and subtle increases in the oxygen vacancy concentration inside the $\mathrm{HfO_2}$, and by adding to the accumulation of electrons in the LSMO. The observation of accurate multi-level resistance control can then finally be explained by the polarization switching with a distribution of switching voltages for various domains inside the film, which gradually changes the electron accumulation in the LSMO, together with a possible minimal contribution from the gradual change of the oxygen vacancy concentration inside the $\mathrm{HfO_2}$, which could have an effect on the barrier height.

Overall, we have demonstrated tuning of the switching behavior in a ferroelectric tunnel junction by ferroelectric polarization switching, and a minimal observation of oxygen vacancy movement. This differs from HZO FTJs, where oxygen vacancies likely have to be stabilized in the HZO crystal structure by the introduction of Zr atoms [77]. Compared with state-of-the-art literature summarized in Table S1, the presented ultra-thin undoped HfO_2 films yield an ON state current several orders of magnitude as high as most HZO FTJs, as well as at least an order of magnitude improvement in endurance and several volts lower write voltage compared with other epitaxial thin films.

4 | Conclusion

In a 3-nm-thin orthorhombic epitaxial ferroelectric tunnel junction comprised of HfO_2 thin films deposited on LSMO/Nb:STO substrates and W top electrodes, we demonstrate high ON currents of 5–42 A/cm^2 at -0.1 to -0.5 V read voltage, low write voltages of ± 3 V, $>10^6$ switching cycles, 16 resistance states, voltage pulse train and spike-timing-dependent plasticity, multi-level neuromorphic functionality, and stable temperature dependence of the switching performance up to 150°C. Direct electron tunneling, with an exponential dependence on the tunneling distance, modulated via electrode carrier depletion due to ferroelectric polarization, is proven to be the switching mechanism. The performance is significantly improved compared with most previously reported epitaxial HZO thin films in terms of ON current, consistent with higher transmission probability through undoped HfO_2, lower write voltage from the low coercive voltage, and superior endurance performance enabled by a stabilized oxygen concentration in the undoped ultra-thin films. Our work highlights the importance of careful materials design in both the ferroelectric film and electrodes for achieving superior FTJ performance of next-generation neuromorphic and analog memory devices.

Acknowledgements

This work was supported by (i) the Engineering and Physical Sciences Research Council (EPSRC, Grant No. EP/Y032942/1), (ii) the Royal Academy of Engineering through the Chair in Emerging Technologies scheme (No. CIET1819_24), (iii) the ERC advanced grant, EU-H2020-ERC-ADG No. 882929, EROS, (iv) the Portuguese Foundation for Science and Technology (FCT) in the framework of the Strategic Funding UID/04650/2025 (DOI: https://doi.org/10.54499/UID/04650/2025), (v) the project M-ERA-NET3/0003/2021 – NanOx4EStor Grant agreement No. 958174 (https://doi.org/10.54499/M-ERA-NET3/0003/2021), (vi) project 2024.12826.MIT (https://doi.org/10.54499/2024.12826.MIT), (vii) project 2024.15998.PEX (https://doi.org/10.54499/2024.15998.PEX), (viii) the FCT for the contract under the FCT Tenure program 1st edition (JPBS), (ix) the Swedish Research Council VR, Grant No. 2021-00357, (x) the Marie Sklodowska-Curie Actions Grant agreement No. 101106176, (xi) the EPSRC Open Fellowship under Grant EP/X011356/1. The authors also thank engineer José Santos for technical support at the Thin Film Laboratory at CF-UM-UP, and Dr. Lei Jin from the Ernst Ruska Centre for Microscopy and Spectroscopy with Electrons, Forschungszentrum Jülich GmbH, Germany, for useful TEM discussions.

Conflicts of Interest

The authors declare no conflicts of interest.

Data Availability Statement

The data that support the findings of this study are openly available in the University of Cambridge repository Apollo with the doi https://doi.org/10.17863/CAM.127881.

References

1. S. Yu and P.-Y. Chen, "Emerging Memory Technologies: Recent Trends and Prospects," *IEEE Solid-State Circuits Magazine* 8 (2016): 43–56, https://doi.org/10.1109/MSSC.2016.2546199.

2. S. Yu, *Semiconductor Memory Devices and Circuits*, 1st ed. (CRC Press, 2022), https://doi.org/10.1201/9781003138747.

3. S. Shiratake, "Scaling and Performance Challenges of Future DRAM," in (*IEEE International Memory Workshop (IMW)* IEEE, 2020), 1–3, https://doi.org/10.1109/IMW48823.2020.9108122.

4. K. Ishimaru, "Challenges of Flash Memory for Next Decade," in 2021 IEEE International Reliability Physics Symposium (IRPS) (IEEE, 2021), 1–5, https://doi.org/10.1109/IRPS46558.2021.9405182.

5. J. Choe, "Memory Technology 2021: Trends & Challenges," (2021): 111–115, https://doi.org/10.1109/SISPAD54002.2021.9592547.

6. A. Mehonic, D. Ielmini, K. Roy, et al., "Roadmap to Neuromorphic Computing with Emerging Technologies," *APL Materials* 12 (2024): 109201, https://doi.org/10.1063/5.0179424.

7. P. Mannocci, M. Farronato, N. Lepri, et al., "In-memory Computing with Emerging Memory Devices: Status and Outlook," *APL Machine Learning* 1 (2023): 010902, https://doi.org/10.1063/5.0136403.

8. D. V. Christensen, R. Dittmann, B. Linares-Barranco, et al., "2022 roadmap on Neuromorphic Computing and Engineering," *Neuromorphic Computing and Engineering* 2 (2022): 022501, https://doi.org/10.1088/2634-4386/ac4a83.

9. A. Sebastian, M. L. Gallo, R. Khaddam-Aljameh, and E. Eleftheriou, "Memory Devices and Applications for in-memory Computing," *Nature Nanotechnology* 15 (2020): 529–544, https://doi.org/10.1038/s41565-020-0655-z.

10. C. D. Schuman, S. R. Kulkarni, M. Parsa, J. P. Mitchell, P. Date, and B. Kay, "Opportunities for Neuromorphic Computing Algorithms and Applications," *Nature Computational Science* 2 (2022): 10–19, https://doi.org/10.1038/s43588-021-00184-y.

11. L. Yin, R. Cheng, Y. Wen, C. Liu, and J. He, "Emerging 2D Memory Devices for in-Memory Computing," *Advanced Materials* 33 (2021): 2007081, https://doi.org/10.1002/adma.202007081.

12. M.-K. Kim, Y. Park, I.-J. Kim, and J.-S. Lee, "Emerging Materials for Neuromorphic Devices and Systems," *Iscience* 23 (2020): 101846, https://doi.org/10.1016/j.isci.2020.101846.

13. M. Hellenbrand, I. Teck, and J. L. MacManus-Driscoll, "Progress of Emerging Non-volatile Memory Technologies in Industry," *MRS Communications* 14 (2024): 1099–1112, https://doi.org/10.1557/s43579-024-00660-2.

14. X. Du, H. Sun, H. Wang, J. Li, Y. Yin, and X. Li, "High-Speed Switching and Giant Electroresistance in an Epitaxial $Hf_{0.5}Zr_{0.5}O_2$-Based Ferroelectric Tunnel Junction Memristor," *ACS Applied Materials & Interfaces* 14 (2022): 1355–1361, https://doi.org/10.1021/acsami.1c18165.

15. V. Garcia and M. Bibes, "Ferroelectric Tunnel Junctions for Information Storage and Processing," *Nature Communications* 5 (2014): 4289, https://doi.org/10.1038/ncomms5289.

16. M. H. Park, Y. H. Lee, T. Mikolajick, U. Schroeder, and C. S. Hwang, "Review and Perspective on Ferroelectric HfO_2-based Thin Films for Memory Applications," *MRS Communications* 8 (2018): 795–808, https://doi.org/10.1557/mrc.2018.175.

17. T. Mikolajick, S. Slesazeck, H. Mulaosmanovic, et al., "Next Generation Ferroelectric Materials for Semiconductor Process Integration and Their Applications," *Journal of Applied Physics* 129 (2021): 100901, https://doi.org/10.1063/5.0037617.

18. T. Mikolajick, U. Schroeder, and S. Slesazeck, "The Past, the Present, and the Future of Ferroelectric Memories," *IEEE Transactions on Electron Devices* 67 (2020): 1434–1443, https://doi.org/10.1109/TED.2020.2976148.

19. K.-H. Kim, I. Karpov, R. H. Olsson, and D. Jariwala, "Wurtzite and Fluorite Ferroelectric Materials for Electronic Memory," *Nature Nanotechnology* 18 (2023): 422–441, https://doi.org/10.1038/s41565-023-01361-y.

20. J. P. B. Silva, R. Alcala, U. E. Avci, et al., "Roadmap on Ferroelectric hafnia- and Zirconia-based Materials and Devices," *APL Materials* 11 (2023): 089201, https://doi.org/10.1063/5.0148068.

21. J. P. B. Silva, K. C. Sekhar, H. Pan, J. L. MacManus-Driscoll, and M. Pereira, "Advances in Dielectric Thin Films for Energy Storage Applications, Revealing the Promise of Group IV Binary Oxides," *ACS Energy Letters* 6 (2021): 2208–2217, https://doi.org/10.1021/acsenergylett.1c00313.

22. F. Ali, D. Zhou, M. Ali, et al., "Recent Progress on Energy-Related Applications of HfO_2-Based Ferroelectric and Antiferroelectric Materials," *ACS Applied Electronic Materials* 2 (2020): 2301–2317, https://doi.org/10.1021/acsaelm.0c00304.

23. M. L. Müller, M. T. Becker, N. Strkalj, and J. L. MacManus-Driscoll, "Schottky-to-Ohmic Switching in Ferroelectric Memristors Based on Semiconducting $Hf_{0.93}Y_{0.07}O_2$ Thin Films," *Applied Physics Letters* 121 (2022): 093501, https://doi.org/10.1063/5.0095762.

24. V. Mikheev, A. Chouprik, Y. Lebedinskii, et al., "Memristor with a Ferroelectric HfO_2 Layer: in which Case It Is a Ferroelectric Tunnel Junction," *Nanotechnology* 31 (2020): 215205, https://doi.org/10.1088/1361-6528/ab746d.

25. U. Schroeder, M. H. Park, T. Mikolajick, and C. S. Hwang, "The Fundamentals and Applications of Ferroelectric HfO_2," *Nature Reviews Materials* 7 (2022): 653–669, https://doi.org/10.1038/s41578-022-00431-2.

26. J. Lee, K. Yang, J. Y. Kwon, et al., "Role of Oxygen Vacancies in Ferroelectric or Resistive Switching Hafnium Oxide," *Nano Convergence* 10 (2023): 55, https://doi.org/10.1186/s40580-023-00403-4.

27. B. Max, M. Pešić, S. Slesazeck, and T. Mikolajick, "Interplay between Ferroelectric and Resistive Switching in Doped Crystalline HfO_2," *Journal of Applied Physics* 123 (2018): 134102, https://doi.org/10.1063/1.5015985.

28. M. L. Müller, N. Strkalj, M. T. Becker, et al., "Stabilizing Schottky-to-Ohmic Switching in HfO_2-Based Ferroelectric Films via Electrode Design," *Advancement of Science* 12 (2025): 2409566, https://doi.org/10.1002/advs.202409566.

29. S. Brivio, S. Spiga, and D. Ielmini, "HfO_2-based Resistive Switching Memory Devices for Neuromorphic Computing," *Neuromorphic Computing and Engineering* 2 (2022): 042001, https://doi.org/10.1088/2634-4386/ac9012.

30. W. Banerjee, A. Kashir, and S. Kamba, "Hafnium Oxide (HfO 2)—A Multifunctional Oxide: a Review on the Prospect and Challenges of Hafnium Oxide in Resistive Switching and Ferroelectric Memories," *Small* 18 (2022): 2107575, https://doi.org/10.1002/smll.202107575.

31. M. Hellenbrand and J. MacManus-Driscoll, "Multi-level Resistive Switching in Hafnium-oxide-based Devices for Neuromorphic Computing," *Nano Convergence* 10 (2023): 44, https://doi.org/10.1186/s40580-023-00392-4.

32. F. Ambriz-Vargas, G. Kolhatkar, M. Broyer, et al., "A Complementary Metal Oxide Semiconductor Process-Compatible Ferroelectric Tunnel Junction," *ACS Applied Material Interfaces* 9 (2017): 13262–13268, https://doi.org/10.1021/acsami.6b16173.

33. Y. Goh, J. Hwang, Y. Lee, M. Kim, and S. Jeon, "Ultra-thin $Hf_{0.5}Z_{r0.5}O_2$ Thin-film-based Ferroelectric Tunnel Junction via Stress Induced Crystallization," *Applied Physics Letters* 117 (2020): 242901, https://doi.org/10.1063/5.0029516.

34. M. Hoffmann, J. A. Murdzek, S. M. George, S. Slesazeck, U. Schroeder, and T. Mikolajick, "Atomic Layer Etching of Ferroelectric Hafnium Zirconium Oxide Thin Films Enables Giant Tunneling Electroresistance," *Applied Physics Letters* 120 (2022): 122901, https://doi.org/10.1063/5.0084636.

35. S. S. Cheema, N. Shanker, C.-H. Hsu, et al., "One Nanometer HfO 2 -Based Ferroelectric Tunnel Junctions on Silicon," *Advanced Electronic Materials* 8 (2022): 2100499, https://doi.org/10.1002/aelm.202100499.

36. K. Lee, J. Byun, K. Park, et al., "Giant Tunneling Electroresistance in Epitaxial Ferroelectric Ultrathin Films Directly Integrated on Si," *Applied Materials Today* 26 (2022): 101308, https://doi.org/10.1016/j.apmt.2021.101308.

37. D. H. Lee, J. E. Kim, Y. H. Cho, et al., "A Fluorite-structured $HfO_2/ZrO_2/HfO_2$ Superlattice Based Self-rectifying Ferroelectric Tunnel Junction Synapse," *Materials Horizons* 11 (2024): 5251–5264, https://doi.org/10.1039/D4MH00519H.

38. S. H. Park, H. J. Lee, M. H. Park, J. Kim, and H. W. Jang, "Ferroelectric Tunnel Junctions: Promise, Achievements and Challenges," *Journal of Physics D: Applied Physics* 57 (2024): 253002, https://doi.org/10.1088/1361-6463/ad33f5.

39. B. Prasad, V. Thakare, A. Kalitsov, Z. Zhang, B. Terris, and R. Ramesh, "Large Tunnel Electroresistance with Ultrathin $Hf_{0.5}Zr_{0.5}O_2$ Ferroelectric Tunnel Barriers," *Advanced Electronic Materials* 7 (2021): 2001074, https://doi.org/10.1002/aelm.202001074.

40. X. Long, H. Tan, F. Sánchez, I. Fina, and J. Fontcuberta, "$Zr_{0.5}O_2$ Tunnel Junctions," *ACS Applied Electronics Materials* 5 (2023): 740–747, https://doi.org/10.1021/acsaelm.2c01186.

41. S. Estandía, J. Gàzquez, M. Varela, et al., "Critical Effect of the Bottom Electrode on the Ferroelectricity of Epitaxial $Hf_{0.5}Zr_{0.5}O_2$ Thin Films," *Journal of Materials Chemistry C* 9 (2021): 3486–3492, https://doi.org/10.1039/D0TC05853J.

42. M. Hellenbrand, "Keysight B2912 Memristor Characterisation," (University of Cambridge, 2024), https://doi.org/10.17863/CAM.109318.

43. A. P. S. Crema, M. C. Istrate, A. Silva, et al., "Ferroelectric Orthorhombic ZrO_2 Thin Films Achieved through Nanosecond Laser Annealing," *Advanced Science* 10 (2023): 2207390, https://doi.org/10.1002/advs.202207390.

44. Y. Luo, Z. Tang, X. Yin, et al., "Ferroelectricity in Dopant-free HfO_2 Thin Films Prepared by Pulsed Laser Deposition," *Journal of Materiomics* 8 (2022): 311–318, https://doi.org/10.1016/j.jmat.2021.09.005.

45. T. Song, R. Bachelet, G. Saint-Girons, R. Solanas, I. Fina, and F. Sánchez, "Thin Films," *ACS Applied Electronics Materials* 2 (2020): 3221–3232, https://doi.org/10.1021/acsaelm.0c00560.

46. P. Jiao, H. Cheng, J. Li, et al., "Flexoelectricity-stabilized Ferroelectric Phase with Enhanced Reliability in Ultrathin La:HfO_2 Films," *Applied Physics Reviews* 10 (2023): 031417, https://doi.org/10.1063/5.0144958.

47. J. P. B. Silva, R. F. Negrea, M. C. Istrate, et al., "Wake-up Free Ferroelectric Rhombohedral Phase in Epitaxially Strained ZrO_2 Thin Films," *ACS Applied Materials & Interfaces* 13 (2021): 51383–51392, https://doi.org/10.1021/acsami.1c15875.

48. Y. Wei, P. Nukala, M. Salverda, et al., "A Rhombohedral Ferroelectric Phase in Epitaxially Strained $Hf_{0.5}Zr_{0.5}O_2$ Thin Films," *Nature Materials* 17 (2018): 1095–1100, https://doi.org/10.1038/s41563-018-0196-0.

49. A. Sawa, "Resistive Switching in Transition Metal Oxides," *Materials Today* 11 (2008): 28–36, https://doi.org/10.1016/S1369-7021(08)70119-6.

50. J. Lyu, I. Fina, J. Fontcuberta, and F. Sánchez, "Epitaxial Integration on Si(001) of Ferroelectric $Hf_{0.5}Zr_{0.5}O_2$ Capacitors with High Retention and Endurance," *ACS Applied Materials & Interfaces* 11 (2019): 6224–6229, https://doi.org/10.1021/acsami.8b18762.

51. C.-Y. Lin, B.-C. Chen, Y.-C. Liu, et al., "Integration of Freestanding Hafnium Zirconium Oxide Membranes into Two-Dimensional Transistors as a High-κ Ferroelectric Dielectric," *Nature Electronics* 8 (2025): 560–570, https://doi.org/10.1038/s41928-025-01398-y.

52. J. S. Kim, N. Strkalj, A. Silva, et al., "Coercive Field Control in Epitaxial Ferroelectric $Hf_{0.5}Zr_{0.5}O_2$ Thin Films by Nanostructure Engineering,"

ACS Applied Material Interfaces 17 (2025): 25442–25450, https://doi.org/10.1021/acsami.4c21787.

53. M. Hellenbrand, B. Bakhit, H. Dou, et al., "Thin Film Design of Amorphous Hafnium Oxide Nanocomposites Enabling Strong Interfacial Resistive Switching Uniformity," *Science Advances* 9 (2023): adg1946, https://doi.org/10.1126/sciadv.adg1946.

54. J.-H. Ryu, F. Hussain, C. Mahata, et al., "Filamentary and Interface Switching of CMOS-Compatible Ta_2O_5 Memristor for Non-Volatile Memory and Synaptic Devices," *Applied Surface Science* 529 (2020): 147167, https://doi.org/10.1016/j.apsusc.2020.147167.

55. Z. Dong, X. Cao, T. Wu, and J. Guo, "Tunneling Current in HfO_2 and $Hf_{0.5}Zr_{0.5}O_2$-Based Ferroelectric Tunnel Junction," *Journal of Applied Physics* 123 (2018): 094501, https://doi.org/10.1063/1.5016823.

56. S. Salahuddin, K. Ni, and S. Datta, "The Era of Hyper-Scaling in Electronics," *Nature Electronics* 1 (2018): 442–450, https://doi.org/10.1038/s41928-018-0117-x.

57. S. Dutta, P. Buragohain, S. Glinsek, et al., "Piezoelectricity in Hafnia," *Nature Communications* 12 (2021): 7301, https://doi.org/10.1038/s41467-021-27480-5.

58. H. Lu, D.-J. Kim, H. Aramberri, et al., "Electrically Induced Cancellation and Inversion of Piezoelectricity in Ferroelectric $Hf_{0.5}Zr_{0.5}O_2$," *Nature Communications* 15 (2024): 860, https://doi.org/10.1038/s41467-024-44690-9.

59. N. Balke, P. Maksymovych, S. Jesse, I. I. Kravchenko, Q. Li, and S. V. Kalinin, "Exploring Local Electrostatic Effects with Scanning Probe Microscopy: Implications for Piezoresponse Force Microscopy and Triboelectricity," *ACS Nano* 8 (2014): 10229–10236, https://doi.org/10.1021/nn505176a.

60. T. Iung, L. Pérez Ramírez, A. Gloskovskii, et al., "Oxygen Vacancy Distribution and Phase Composition in Scaled, $Hf_{0.5}Zr_{0.5}O_2$-Based Ferroelectric Capacitors," *Applied Physics Letters* 126 (2025): 062903, https://doi.org/10.1063/5.0245595.

61. P. Nukala, M. Ahmadi, Y. Wei, et al., "Reversible Oxygen Migration and Phase Transitions in Hafnia-Based Ferroelectric Devices," *Science* 372 (2021): 630–635, https://doi.org/10.1126/science.abf3789.

62. W. Shen, R. Dittmann, U. Breuer, and R. Waser, "Improved Endurance Behavior of Resistive Switching in (Ba,Sr)TiO_3 Thin Films with W Top Electrode," *Applied Physics Letters* 93 (2008): 222102, https://doi.org/10.1063/1.3039809.

63. D. Cooper, C. Baeumer, N. Bernier, et al., "Anomalous Resistance Hysteresis in Oxide ReRAM: Oxygen Evolution and Reincorporation Revealed by in Situ TEM," *Advanced Materials* 29 (2017): 1700212, https://doi.org/10.1002/adma.201700212.

64. D. Pantel and M. Alexe, "Electroresistance Effects in Ferroelectric Tunnel Barriers," *Physical Review B* 82 (2010): 134105, https://doi.org/10.1103/PhysRevB.82.134105.

65. S. Monaghan, P. K. Hurley, K. Cherkaoui, M. A. Negara, and A. Schenk, "Determination of Electron Effective Mass and Electron Affinity in HfO_2 Using MOS and MOSFET Structures," *Solid-State Electronics* 53 (2009): 438–444, https://doi.org/10.1016/j.sse.2008.09.018.

66. G. N. Derry, M. E. Kern, and E. H. Worth, "Recommended Values of Clean Metal Surface Work Functions," *Journal of Vacuum Science & Technology A: Vacuum, Surfaces, and Films* 33 (2015): 060801, https://doi.org/10.1116/1.4934685.

67. A. Wratten, S. L. Pain, D. Walker, et al., "Mechanisms of Silicon Surface Passivation by Negatively Charged Hafnium Oxide Thin Films," *IEEE Journal of Photovoltaics* 13 (2023): 40–47, https://doi.org/10.1109/JPHOTOV.2022.3227624.

68. V. V. Afanas'ev and A. Stesmans, "Internal Photoemission at Interfaces of High-κ Insulators with Semiconductors and Metals," *Journal of Applied Physics* 102 (2007): 081301, https://doi.org/10.1063/1.2799091.

69. H.-S. Lee and H.-H. Park, "Band Structure Analysis of $La_{0.7}Sr_{0.3}MnO_3$ Perovskite Manganite Using a Synchrotron," *Advances in Condensed Matter Physics* 2015 (2015): 1, https://doi.org/10.1155/2015/746475.

70. H. Dou, N. Strkalj, Y. Zhang, J. L. MacManus-Driscoll, Q. Jia, and H. Wang, "Optical Dielectric Properties of HfO_2-based Films," *Journal of Vacuum Science & Technology A* 40 (2022): 033412, https://doi.org/10.1116/6.0001651.

71. W. Shin, C.-H. Han, J. Kim, R.-H. Koo, K. K. Min, and D. Kwon, "Effects of Charge Imbalance on Field-Induced Instability of HfO_2-Based Ferroelectric Tunnel Junctions," *Advanced Electronic Materials* 11 (2025): 2400299, https://doi.org/10.1002/aelm.202400299.

72. W. Shin, J.-H. Bae, D. Kwon, et al., "Investigation of Low-Frequency Noise Characteristics of Ferroelectric Tunnel Junction: from Conduction Mechanism and Scaling Perspectives," *IEEE Electron Device Letters* 43 (2022): 958–961, https://doi.org/10.1109/LED.2022.3168797.

73. C. W. Jen, C. L. Lee, and T. F. Lei, "Depletion Widths of the Metal-insulator Semiconductor (MIS) Structure," *Solid-State Electronics* 24 (1981): 949–954, https://doi.org/10.1016/0038-1101(81)90116-7.

74. A. N. Morozovska, E. A. Eliseev, S. V. Svechnikov, et al., "Finite Size and Intrinsic Field Effect on the Polar-Active Properties of Ferroelectric-Semiconductor Heterostructures," *Physical Review B* 81 (2010): 205308, https://doi.org/10.1103/PhysRevB.81.205308.

75. I. Bergenti, V. Dediu, E. Arisi, et al., "Spin Polarized $La_{0.7}Sr_{0.3}MnO_3$ Thin Films on Silicon," *Journal of Magnetism and Magnetic Materials* 312 (2006): 453–457, https://doi.org/10.1016/j.jmmm.2006.11.221.

76. L. Pintilie and M. Alexe, "Metal-Ferroelectric-Metal Heterostructures with Schottky Contacts. I. Influence of the Ferroelectric Properties," *Journal of Applied Physics* 98 (2005): 124103, https://doi.org/10.1063/1.2148622.

77. M. Materano, T. Mittmann, P. D. Lomenzo, et al., "Layers," *ACS Applied Electronic Materials* 2 (2020): 3618–3626, https://doi.org/10.1021/acsaelm.0c00680.

Supporting Information

Additional supporting information can be found online in the Supporting Information section.

Supporting File: adfm74667-sup-0001-SuppMat.pdf.